Multiple microscopy modalities applied to a sea urchin tooth fragment

S. R. Stock,[a]* K. Ignatiev,[b] T. Dahl,[c] J. Barss,[c] K. Fezzaa,[d] A. Veis,[c] W. K. Lee[d] and F. De Carlo[d]

[a]Institute for Bioengineering and Nanoscience in Advanced Medicine, Ward 13-130, Northwestern University, 303 East Chicago Avenue, Chicago, IL 60611-3008, USA, [b]School of Materials Science and Engineering, 711 Ferst Drive, Georgia Institute of Technology, Atlanta, GA 30332-0245, USA, [c]Department of Cell and Molecular Biology, Ward 13-100, Northwestern University, 303 East Chicago Avenue, Chicago, IL 60611, USA, and [d]Advanced Photon Source, 9700 South Cass Avenue, Argonne National Laboratory, Argonne, IL 60439, USA. E-mail: s-stock@northwestern.edu

Two synchrotron X-ray microscopy methods, phase-contrast microradiography (the propagation method) and absorption microCT (high-resolution computed tomography or microtomography), and laser-scanning confocal microscopy (visible wavelength) were used to study a fragment of the keel of a tooth of the sea urchin *Lytechinus variegatus*. Stripes observed in the phase-contrast images of the fragment were also seen in confocal micrographs. MicroCT showed that the stripes were due to two parallel planar arrays of low-absorption channels within the bulk of the keel. In the phase microradiographs, maximum contrast stripes appear when a channel image from one row coincides with a channel image from the second row; otherwise, contrast is minimal. Long channels do not appear to have been observed previously in keels of sea urchin teeth.

Keywords: sea urchins; teeth; X-ray microCT; X-ray phase contrast; calcite; keel; computed tomography.

1. Introduction

The spatial resolution and contrast sensitivity of synchrotron X-radiation-based techniques such as absorption microCT (micro-computed tomography) or phase-contrast imaging have revealed unsuspected aspects of inorganic and biogenic materials (*e.g.* Lee *et al.*, 1998; Guvenilir & Stock, 1998; Ludwig *et al.*, 2003; Kinney *et al.*, 2000; Momose *et al.*, 1996, 2000; Arfelli *et al.*, 1998). The possibility of repeated noninvasive interrogation of volumes of material has re-oriented thinking on how engineered materials can be improved and how the function of materials or tissues can be better understood.

The heavy demand for X-ray beam time dictates that Edisonian characterization strategies, *i.e.* examining multitudes of samples in the hope that something interesting will be seen, are simply impractical at synchrotron radiation sources. Synchrotron microCT is one example of this. When the data described below were collected, $\sim$2 h was required to acquire data to reconstruct 1 mm^3 volumes. Several minutes sufficed for collecting absorption or phase microradiographs at a number of different orientations, and, despite the loss of three-dimensional information inherent in this projection technique, surveying samples of potential interest for more detailed interrogation is very valuable.

The investigation related below began with a synchrotron X-ray phase microradiographic survey of sea urchin ossicles (*i.e.* the structural analogs of chordate bone); a curious pattern of contrast was observed in a tooth fragment. Confocal-light microscopy was next applied and showed that the X-ray phase contrast did not originate solely from surface topography. Finally, synchrotron absorption microCT revealed the three-dimensional structures responsible for the unusual contrast in the phase microradiographs.

Earlier X-ray tube-based microCT (lower spatial resolution, lower contrast sensitivity) revealed nothing inconsistent with conventional understanding of the structure (Stock, Dahl *et al.*, 2002; Stock, Barss *et al.*, 2002), and, in the absence of the phase radiographs, it would not have occurred to one that synchrotron microCT of the more heavily mineralized sections of the keel would be at all worthwhile. It is unlikely that the relevant volume would have been serially sectioned in its natural state because the mineral phase does not section well; if the sample were sectioned, the features identified in the present structure would have been ascribed to an artefact of pull-out during sectioning. Thus, this investigation, a progression of multiple microscopy modes applied to a fragment of sea urchin tooth, documents a process which perhaps should be applied more often.

2. Background

Sea urchin teeth contain structures evolved to enhance feeding efficiency. These complex biocomposites employ highly aligned calcite crystal reinforcements ranging in morphology from plates to thin lamellae to needles to long prisms or fibers. Not only do microstructural scale and reinforcement morphology vary, but developmental gradients also exist: teeth grow continuously from one end, gain mineral through their midsection and self-sharpen at the other. Various sea urchin species emphasize different reinforcement mechanisms to meet the particular requirements of their ecological niches, and there have been a number of excellent studies of various aspects of sea urchin tooth development and functionality (Märkel & Titschak, 1969; Märkel, 1969; Märkel *et al.*, 1989; Candia Carnevali *et al.*, 1991; Wang *et al.*, 1997). Newly available X-ray imaging modalities offer fresh approaches to characterizing the microstructure of sea urchin teeth and, because of the penetrating nature of X-radiation, may eventually develop into powerful *in vivo* probes of invertebrate and vertebrate mineralization.

One of these X-ray methods for detecting differences in X-ray absorptivity is high-resolution X-ray computed tomography (*i.e.* X-ray microtomography or microCT). X-ray absorption microCT, pioneered in the last half of the 1980s, combines views through the sample from various directions into a cross-sectional map of X-ray absorption. With laboratory sources of X-radiation, spatial resolutions can approach 10–20 µm; with synchrotron X-radiation, achieving a resolution below 2 µm is not uncommon [see for example the papers in Bonse (2002)]. Further details and applications of microCT can be found elsewhere (Stock, 1999).

X-ray phase-contrast imaging is a second method which finds its principal application with synchrotron radiation; it offers considerably greater sensitivity than absorption-based techniques for many samples, particularly those containing different types of soft tissue. The origin of the wavefront distortion (*i.e.* phase shift) which produces contrast can be different thicknesses of material traversed by the X-ray beam at different positions or varying index of refraction within the sample. Alternatives for phase-contrast imaging include: X-ray interferometry for direct measurement of phase shift (*e.g.* Beckmann *et al.*, 1999; Bonse & Beckmann, 2001; Momose *et al.*, 1999; Momose, 2002), crystal analyzers for detection of shifts in the X-ray propagation direction (*e.g.* Davis *et al.*, 1995; Chapman *et al.*, 1997) and the 'in-line' or 'propagation' method for Fresnel diffraction of the sample (*e.g.* Snigerev *et al.*, 1995; Cloetens *et al.*, 1996, 1999; Ludwig *et al.*, 2003).

Initial laboratory microCT studies of the keeled teeth of the sea urchin *Lytechinus variegatus* revealed two bands of low absorption within the fully mineralized keel and parallel to its sides (Stock, Dahl *et al.*, 2002; Stock, Barss *et al.*, 2002). The same study employed phase-contrast microradiography of an entire tooth immersed in fluid. In the developing keel, phase microscopy disclosed striations running from the flange to the base of the keel (see Fig. 1) thought to be related to early stages of calcite prism formation, but there was only a hint of structure visible in the fully mineralized portion of the keel adjacent to the cutting edge of the tooth. Apparently the presence of the fluid and the curved plastic vial degraded phase contrast in the denser portions of the keel. The original intent of the study reported below was to eliminate this effect by imaging a keel fragment without surrounding fluid or container. Initially, changes in contrast were not noted between phase microradiographs recorded at different sample orientations (with respect to the incident X-ray beam). Uncovering the origin of the phase contrast required application of confocal optical microscopy and synchrotron X-ray absorption microCT to the same specimen.

3. Methods, results and discussion

A millimeter-sized fragment of the keel was cleaved from the highly mineralized section of a *Lytechinus variegatus* tooth. As indicated schematically in Fig. 1, the irregular parallelepiped-shaped fragment extended neither to the flange nor to the base of the keel but did encompass the entire thickness of the keel.

X-ray phase-contrast microradiographs of the fragment were recorded at various sample orientations at station 1-ID at the APS (Advanced Photon Source) using the propagation method and the following parameters: 30 keV photon energy, a 1 K × 1 K CCD detector coupled optically to a 300 µm-thick $CdWO_4$ scintillator screen and a sample–detector separation of 405 mm. Fig. 2 shows a typical phase-enhanced image of the fragment formed with 3.9 µm pixels. Contrast was dominated by an array of uniformly spaced dark stripes (labeled 1), but a weaker set of stripes (2) overlapped those of set 1 in some places and was present in areas where the stripes of set 1 were absent. The stripes of set 1 averaged about 12 µm in width, their centers were about 21 µm apart and these varied enough from position to position that it is unreasonable to quote values to better than 1 µm (*i.e.* one-quarter of a pixel). The contrast of stripe set 2 was too poor for meaningful quantification.

The contrast of the two sets of stripes appears to be qualitatively different in the phase image of Fig. 2; and rotation about the axis indicated by the unlabeled arrow in Fig. 2 (*i.e.* the vertical axis in the frame of reference of the storage ring) produced neither an increase in prominence in the stripes of set 2 nor a decrease in contrast of set 1. Rotation about a second axis (perpendicular to the first and to the incident beam) also produced no change in the pattern of stripes. These rotation data suggest that the origins of the two sets of stripes were different. Based upon descriptions of the keel morphology (*e.g.* Märkel, 1969), changes in X-ray path between adjacent carinar process plates are expected to produce gross changes in the pattern of contrast for at least some combinations of rotations. Either the contrast was not due to the array of carinar process plates or it was due to some difficult-to-fathom phase effect.

Following phase imaging, the surface of the fragment was observed using a low-magnification stereomicroscope using oblique lighting. Stripe-like features were weakly visible, paralleling those seen in the phase images. Optical confocal microscopy was performed to document the visual observations. A Zeiss LSM510 Laser Scanning Confocal Microscope with a red HeNe laser source was used to image the fragment, and the orientation and magnification of the images in Fig. 3 were selected to correspond to the phase image of Fig. 2. Figs. 3(*a*) and 3(*b*) were produced by focusing at two different heights and show differences in contrast that are similar to that seen in the phase image of Fig. 2. Note that the area in contrast in Fig. 3(*a*) matches sections *C* and *C′* in Fig. 2 and that in Fig. 3(*b*) matches *D* in Fig. 2; the contrast within these portions of the phase images must, therefore, originate within volumes or at surfaces at two well defined heights.

The pattern of stripes from the visible-light images of *D* agrees, at least qualitatively, with those in the phase image. In Fig. 3(*b*), thick streaks alternate with thin streaks, the thin streaks appear to lie midway between thick streaks, the spacing between thick streaks is about 30–40 µm and the pattern of streaks is much less regular than that of the stripes in the phase image of Fig. 2. The pattern of contrast in regions *C* and *C′* (Fig. 3*a*) is even more complex than that in *D*. The fine pattern of streaks appears to be absent. Some coarse streaks in *C* appear to parallel those in *D* and have a similar period, and wider rather irregular streaks follow stripe set 2 of Fig. 2. The visible-light data confirm that the various stripes in the phase image do not originate as an obscure artefact of phase imaging but are features of

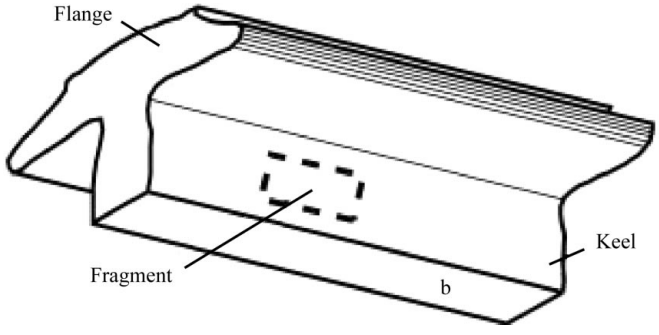

Figure 1
Schematic of the midshaft section of a tooth of *Lytechinus variegatus*. The keel fragment came from a position like that outlined by the dashed line, and b denotes the base of the keel.

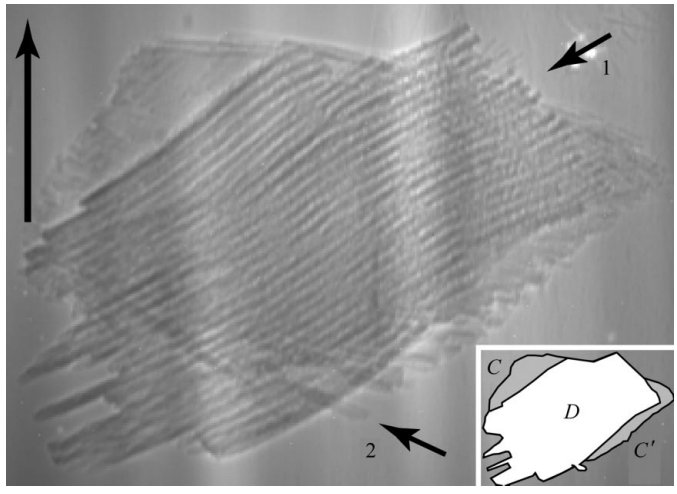

Figure 2
Phase-enhanced X-ray microradiography of the keel fragment produced with the X-ray beam almost normal to the surface of the specimen. Darker pixels represent lower intensities, and the horizontal field of view is 1.20 mm. The inset schematic identifies fragment sections *D* (white area) associated with stripe set 1 and *C* and *C′* (shaded area) with stripe set 2.

the fragment tied to different portions of its volume. In order to shed more light on the three-dimensional positions of the stripes on/within the fragment, the investigators attempted to obtain confocal images from planes other than those in Fig. 3 (calcite varies from translucent biogenic material to highly transparent inorganic material), but the images were so complex that an alternative approach, described below, was employed.

The spacing and widths of the streaks observed dictate that synchrotron (absorption) microCT is required to resolve the individual features present in the phase-enhanced and optical images. Data for computed tomographic reconstruction of the keel fragment were collected at station 2-BM at APS (Wang *et al.*, 2001) using 14 keV photons, a 1.33 mm × 1.33 mm field of view, a 1 K × 1 K CCD detector coupled optically to a 500 µm-thick $CdWO_4$ crystal and views every 0.25° over a range of 180°. The reconstructed slices were normal to the plane of Fig. 2 and parallel to the rotation axis used for the phase imaging (unlabeled arrow in Fig. 2).

Fig. 4 shows a typical slice of the keel fragment, reconstructed on a 512 × 512 grid with 2.6 µm isotropic voxels (volume elements). Two rows of low-absorption features (*A* and *B* in Fig. 4) are visible within the fragment, and the rows are separated by between 140 µm and 150 µm. Fig. 5 shows three-dimensional views of the structure within a small portion of the fragment and reveals that the low-absorption features are tube-like channels running through its length and parallel to its sides. The left-hand image of Fig. 5 was formed by numerically sectioning the reconstructed volume (of the fragment) along three orthogonal planes. The gray scale is the same as in Fig. 4. The right-hand image of Fig. 5 is a three-dimensional rendering showing only the low-absorption voxels within the volume shown at the left of Fig. 5. The double-headed arrows link the same row of channels in the two different representations; the rear row of channels is seen particularly clearly. Small linear features with alternating light and dark pixels are seen both in slices (Fig. 4) and on the surfaces of the gray scale volume (*E* and *E′* in Fig. 5). The rendering

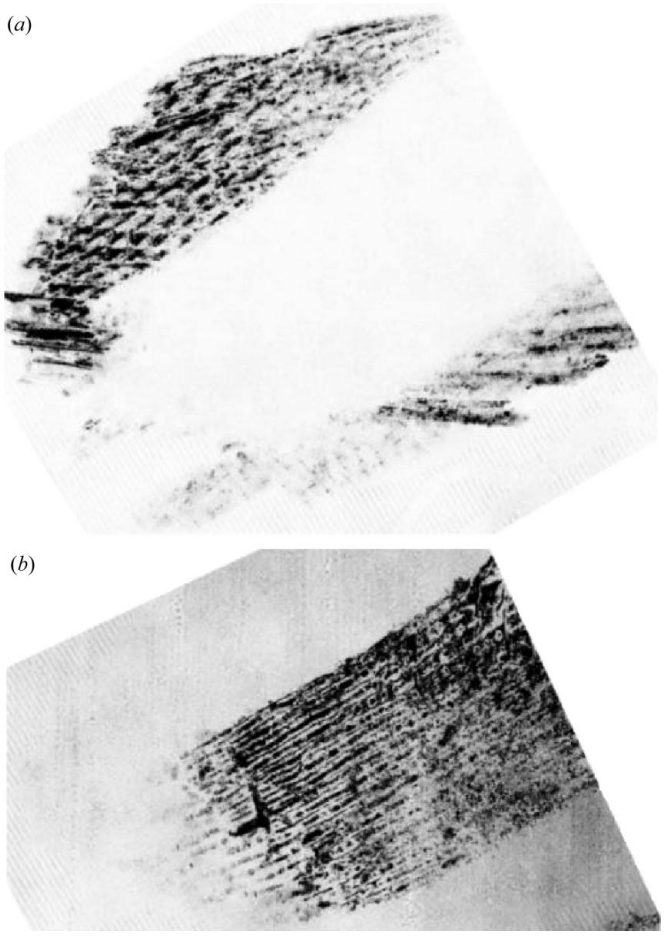

Figure 3
Laser-scanning confocal-light micrographs of the keel fragment from the same viewing direction as in Fig. 2. The images shown in (*a*) and (*b*) were formed by focusing the beam at different heights, and both were reproduced to approximate the scale of Fig. 2.

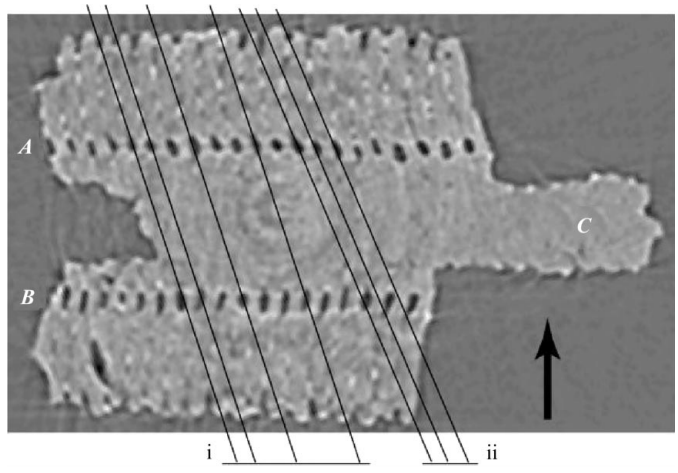

Figure 4
Synchrotron absorption microCT slice of the keel fragment (the darker the pixel, the lower the absorptivity of the corresponding voxel). The unlabeled arrow shows the approximate viewing perspective for Figs. 2 and 3. The vertical field of view is 0.78 mm.

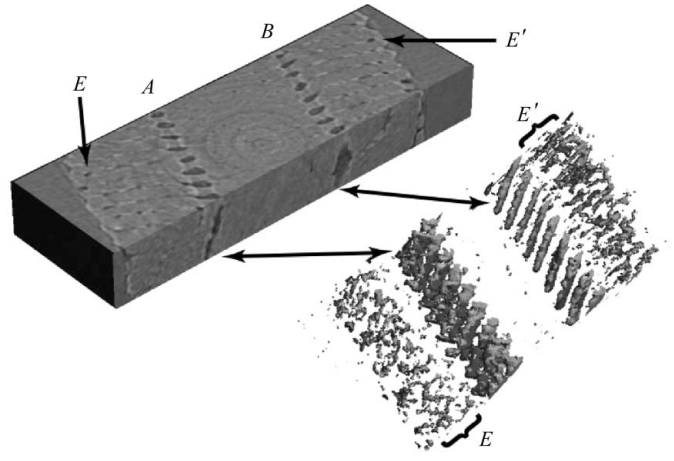

Figure 5
Three-dimensional renderings derived from a subset of the reconstructed volume which spans the thickness of the keel (upper and lower borders in Fig. 4). *A* and *B* correspond to the rows of channels described in Fig. 4. The upper-left rendering shows lower-absorbing voxels with darker pixels, and the edges of the parallelepiped are 49, 120 and 365 µm in length. The rendering at the lower right shows only the lowest-absorption voxels (dark gray pixels) with black indicating shadows; all voxels more absorbing than the channels are rendered transparent. The double-headed arrows point to the same row of channels in the other rendering. Note that the viewing perspective changes between the renderings; this is necessary to allow the separation between channels of one row to be seen clearly due to the fact that the channels have an elliptical cross section.

of the low-absorption voxels (right-hand image of Fig. 5) fails, however, to capture the pattern of features *E* and *E′*.

Viewed from the direction indicated by the arrow, the top-most edge of the sample in the slice shown in Fig. 4 is part of a surface of two discrete levels; this would produce two-level images like those seen in the confocal micrographs of Fig. 3. The microCT slices show both surfaces (top and bottom edges of the sample in a single slice) of the fragment to be corrugated with a roughness approaching that of the diameter of the channels and spacing similar to that observed in the phase-enhanced images. Inspection of slices adjacent to that in Fig. 4 reveals that the surface corrugations are not long enough to produce the stripes in fragment region *D* (Fig. 2).

The spacing and width of the channels in the microCT data (about 20 μm and 10 μm, respectively) dictate that the stripes in region *D* of the phase-contrast images cannot be due to the simple projection of the pair of channel rows. The largest change in contrast, *i.e.* the most prominent stripes, must occur along views where the images of channel row *A* superimpose on those of row *B* (Fig. 4); further, along viewing directions almost perpendicular to the row of channels, 'unobstructed' paths exist through the matrix of the fragment. Because the channels wander slightly and have slightly irregular shapes, such a contrast mechanism would inevitably produce Moiré-like effects in a phase image of the keel; such appears to be the case at various positions in Fig. 2.

If the stripes in the phase radiograph are produced by alignment of the channels, then rotation of the sample should produce changes in the pattern of stripes. The two sets of narrow lines in Fig. 4 illustrate how this might occur: along viewing direction (i) the channels through which the narrow lines pass are aligned while the channels are offset after 5° rotation to viewing direction (ii). The enlargements in Fig. 6 show that this happens in phase images of the keel fragment. Fig. 6(*a*) is from the upper center region of the image in Fig. 2, and Fig. 6(*b*) shows the same area after 5° rotation. The numbers 1 and 5 mark the first and fifth stripes, respectively, in Fig. 6(*a*), and white dots are used to indicate the positions of the stripes between 1 and 5. Note that there are five stripes to the left of the edge *e* of the larger section of the fragment. The stripes to the left of *e* are labeled in Fig. 6(*b*), but there are only four stripes visible (three dots to the right of 1).

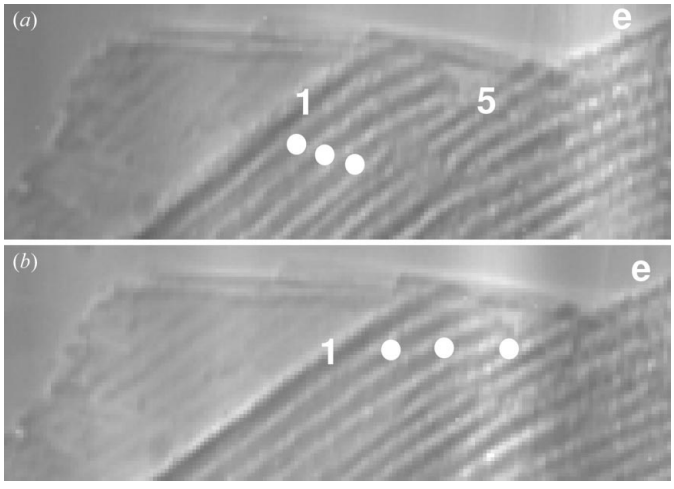

Figure 6
Enlargements of the upper central portion of the phase-enhanced image shown in Fig. 2 (*a*) and an image produced after a 5° rotation (*b*). The contrast is the same as in Fig. 2, the full width of the stripes is about 12 μm and the symbols are explained in the text.

Sequential viewing of the microCT slices of the fragment shows that region C of the phase radiograph (Fig. 2) corresponds to the portion of the fragment labeled *C* in the microCT slice shown in Fig. 4. Material between the surface and the remaining material comprising *C* (and containing channels) appears to have fractured from the fragment. Some roughness is visible on the surface of *C* and may be the origin of the streaks paralleling stripe set 1 of the phase image (Fig. 2). Other slices, not included, show that the coarse stripes of set 2 of the phase image are long prism-like pieces of the keel partially fractured from the edge of the fragment.

Synchrotron X-ray phase microCT would perhaps have been a more logical follow-on to the phase microradiography than absorption microCT, but capabilities did not and still do not exist at the APS beamlines at which the authors have access. Note that propagation-based phase microCT cannot yet be performed on 1-ID because of beam jitter, and algorithms for propagation-based microCT reconstruction (Cloetens *et al.*, 1999) remain to be implemented at 2-BM.

Laboratory microCT performed prior to the present investigation revealed a pair of indistinct low-attenuation zones apparently at the borders of the carinar processes on either side of the central prism region in the teeth of *Lytechnius variegatus*. These zones appeared to fade into and out of the background of the ossicle, and this was attributed to slight changes in mineral density at the transition between the prism region and the carinar process. As is now apparent, the spatial resolution and contrast sensitivity with the laboratory system were too low to reveal the presence of the rows of channels. Without the interesting structure observed in the phase-contrast images of the developing keel and of the mature keel fragment and confirmed *via* confocal-light microscopy, it is unlikely that synchrotron microCT of the keel would have been deemed worthwhile. Only with the application of multiple microscopy modes did the actual channel structure emerge, a structure which does not appear to have been noted previously in sea urchin teeth.

The authors thank Weiming Yu for his instruction on the use of the confocal microscope, and acknowledge the use of the facilities of the Cell Imaging Facility, Department of Cell and Molecular Biology, Northwestern University. Research on sea urchin teeth was supported by NIDCR grants K08-DE00424, DE07201 and DE01374. The phase-contrast imaging and synchrotron absorption microCT were performed at the facilities of SRI-CAT of APS, supported by the DOE under contract W-31-109-Eng-38.

References

Arfelli, F., Assante, M., Bonvicini, V., Bravin, A., Cantatopre, G., Castelli, E., Dalla Palma, L., Di Michiel, M., Longo, R., Olivo, A., Pani, S., Pontoni, D., Poropat, P., Prest, M., Rashevsky, A., Tramba, G., Vacchi, A., Vallazza, E. & Aonconati, F. (1998). *Phys. Med. Biol.* **43**, 2845–2852.
Beckmann, F., Bonse, U. & Biermann, T. (1999). *Proc. SPIE*, **3772**, 179–187.
Bonse, U. (2002). *Proc. SPIE*, **4503**.
Bonse, U. & Beckmann, F. (2001). *J. Synchrotron Rad.* **8**, 1–5.
Candia Carnevali, D. M., Bonasoro, F. & Melone, G. (1991). *Bull. Zool.* **58**, 1–42.
Chapman, D., Thomlinson, W., Johnson, R. E., Washburn, D., Pisano, E., Gmür, N., Zhong, Z., Menk, R., Arfelli, F. & Sayers, D. (1997). *Phys. Med. Biol.* **42**, 2015–2025.
Cloetens, P., Barrett, R., Baruchel, J., Guigay, J. P. & Schlenker, M. (1996). *J. Phys. D*, **29**, 133–146.
Cloetens, P., Ludwig, W., Baruchel, J., Van Dyck, D., Van Landuyt, J., Guigay, J. P. & Schlenker, M. (1999). *Appl. Phys. Lett.* **75**, 2912–2914.
Davis, T. J., Gao, D., Gureyev, T. E., Stevenson, A. W. & Wilkins, S. W. (1995). *Nature (London)*, **373**, 595–598.

Guvenilir, A. & Stock, S. R. (1998). *Fatigue Fract. Eng. Mater. Struct.* **21**, 439–450.
Kinney, J. H., Haupt, D. L., Balooch, M., Ladd, A. J. C., Ryaby, J. T. & Lane, N. E. (2000). *J. Bone Miner. Res.* **15**, 1981–1991.
Lee, S. B., Stock, S. R., Butts, M. D., Starr, T. L., Breunig, T. M. & Kinney, J. H. (1998). *J. Mater. Res.* **13**, 1209–1217.
Ludwig, W., Buffiere, J. Y., Savelli, S. & Cloetens, P. (2003). *Acta Mater.* **51**, 585–598.
Märkel, K. (1969). *Z. Morph. Tiere*, **66**, 1–50.
Märkel, K., Röser, U. & Stauber, M. (1989). *Zoomorphology*, **109**, 79–87.
Märkel, K. & Titschack, H. (1969). *Z. Morph. Tiere*, **64**, 179–200.
Momose, A. (2002). *J. Synchrotron Rad.* **9**, 136–142.
Momose, A., Takeda, T. & Itai, Y. (2000). *Radiology*, **217**, 593–596.
Momose, A., Takeda, T., Itai, Y. & Hirano, K. (1996). *Nature Med.* **2**, 473–475.
Momose, A., Takeda, T., Itai, Y., Tu, J. & Hirano, K. (1999). *Proc. SPIE*, **3772**, 188–195.
Snigerev, A., Snigereva, I., Kohn, V., Kuznetsov, S. & Schelokov, I. (1995). *Rev. Sci. Instrum.* **66**, 5486–5492.
Stock, S. R. (1999). *Inter. Mater. Rev.* **44**, 141–164.
Stock, S. R., Barss, J., Dahl, T., Veis, A. & Almer, J. D. (2002). *J. Struct. Biol.* **139**, 1–12.
Stock, S. R., Dahl, T., Barss, J., Veis, A., Fezzaa, K. & Lee, W. K. (2002). *Adv. X-ray Anal.* **45**, 133–138.
Wang, R. Z., Addadi, L. & Weiner, S. (1997). *Philos. Trans. R. Soc. London*, B**352**, 469–480.
Wang, Y., De Carlo, F., Mancini, D., McNulty, I., Tieman, B., Bresnahan, J., Foster, I., Insley, J., Lane, P., von Laszewski, G., Kesselman, C., Su, M.-H. & Thiebaux, M. (2001). *Rev. Sci. Instrum.* **72**, 2062–2068.

 Received 25 November 2002 • Accepted 23 June 2003